Macromolecules

pubs.acs.org/Macromolecules Article

Design of Polymer Blend Electrolytes through a Machine Learning Approach

Bill K. Wheatle, Erick F. Fuentes, Nathaniel A. Lynd, and Venkat Ganesan*

Cite This: *Macromolecules* 2020, 53, 9449–9459 Read Online

ACCESS | Metrics & More | Article Recommendations | Supporting Information

ABSTRACT: We apply a machine learning (ML) technique to the multiobjective design of polymer blend electrolytes. In particular, we are interested in maximizing electrolyte performance measured by a combination of ionic transport (measured by ionic conductivity) and electrolyte mechanical properties (measured by viscosity) in a coarse-grained molecular dynamics framework. Recognizing the expense of evaluating each of these properties, we identify that the anionic mean-squared displacement and polymer relaxation time can serve as their proxies. By employing the ML approach known as Bayesian optimization, we identify a trade-off between ion transport and electrolyte mechanical properties as a function of varied design parameters, which include host molecular weight and polarity. Our results suggest that blend electrolytes whose hosts have unequal molecular weights, such as gel polymer electrolytes, rarely maximize electrolyte performance. Overall, our results suggest the potential of a framework to design high-performance electrolytes using a combination of molecular simulation and ML.

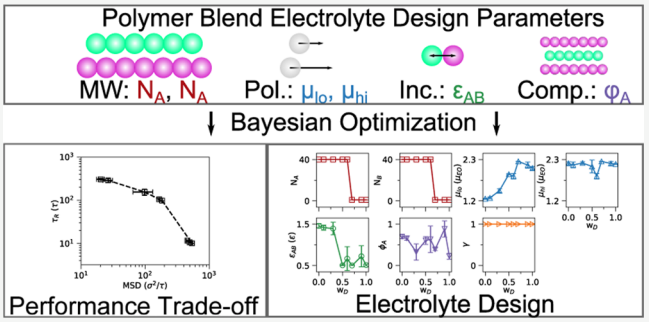

Downloaded via UNIV OF TEXAS AT AUSTIN on August 2, 2021 at 15:03:57 (UTC).
See https://pubs.acs.org/sharingguidelines for options on how to legitimately share published articles.

1. INTRODUCTION

Lithium-ion batteries (LIBs) are emerging as a part of the comprehensive solution to climate change by assisting integration of renewable electricity into the grid.[1−3] Although LIBs are commercially successful, efforts have been made to improve their energy and power densities by replacing their graphitic anodes with lithium metal.[4−7] However, dendrites formed from uneven stripping and deposition of lithium ions have limited the adoption of lithium-metal batteries.[4] It has been suggested that reducing the counteranion mobility[8] and/or increasing the electrolyte shear modulus[9] may alleviate the issue of dendrite formation.

In this regard, polymeric electrolytes are emerging as high-performance materials that can enable such objectives. Indeed, appending the counterion to a polymer host has been shown to significantly reduce its mobility.[10−15] Further, by simply tuning the molecular weight of the polymer host, the shear modulus of the resulting material can be increased.[16−18] Despite their advantages, polymer electrolytes exhibit sluggish ionic transport, limited by a competition between ionic aggregation[19−24] and slow polymer dynamics.[25−30] As a result of such observations, it is becoming clear that polymer electrolyte design is one involving multiple performance metrics, which may be in competition with each other. In this work, we chose to design electrolytes on the basis of comaximizing ionic transport and polymer dynamics.

Design of polymer electrolytes on this basis has primarily advanced through physical intuition guiding the choice of different properties to promote ion transport while maintaining sufficient mechanical integrity.[19−25,25−32] In contrast, machine learning (ML) techniques have been applied in a variety of application areas in materials science,[33−40] including polymer physics,[41−49] to design materials which possess the optimal combination of desired properties. Inspired by such successes, we present results using ML in combination with molecular dynamics simulations as a means to design polymer electrolytes.

The context for the present study arises from our recent work in which we identified that miscible polymer blend electrolytes (PBEs) consisting of high-mobility and high-polarity components may potentially modulate the trade-off between ion aggregation and polymer dynamics. In some instances, these PBEs were shown to have faster ion transport than electrolytes whose hosts consisted only of a single polymer type. However, the study was limited in scope: elements of the design space, such as host molecular weights and host polarities, were restricted, and no attention was paid to the influence of design parameters on the overall mechanical properties.[31] The parameter space accompanying polymer blend systems is extensive and includes molecular weight and

Received: July 5, 2020
Revised: September 29, 2020
Published: October 21, 2020

ACS Publications © 2020 American Chemical Society

https://dx.doi.org/10.1021/acs.macromol.0c01547
Macromolecules 2020, 53, 9449−9459

polarity contrast between the two components and the regime of miscibility characterizing the blend components. This renders an exhaustive study of the dependence of the desired properties on the different parameters to identify the optimal combination an intractable task. Motivated by such challenges, in this study, we explored the use of one ML approach to comprehensively examine the potential of PBEs to simultaneously improve ionic transport and mechanical properties.

Toward the above objective, we identified two performance metrics of interest:

1. We discuss the electrolyte's ionic conductivity λ, which measures the rate of ionic transport under a given applied electric field. Assuming a monovalent, binary salt, λ can be expressed in the following form[50]

$$\lambda = \alpha \frac{ne^2}{Vk_BT}(D_c + D_a) \tag{1}$$

where e is the proton charge, V is the system volume, k_B is the Boltzmann constant, T is the temperature, and n is the number of cations. D_c and D_a are the cationic and anionic diffusivities, respectively, measuring self-correlated ionic motion. The degree of uncorrelated motion α captures the extent to which distinct ionic motion is correlated.

2. While the methodology and framework presented in this article are general enough to accommodate any characteristic mechanical property, in this work, we explored the use of the material viscosity and polymer segmental dynamics as the feature competing against the maximization of ionic transport. We note that there has arisen significant recent interest in understanding and exploiting the "decoupling" between polymer dynamics and ion transport in a variety of other contexts.[51−55] Because of the slow dynamics of the system, influenced in part by the presence of ions, it is computationally difficult to probe the long-time zero shear viscosity \enleadertwodots.[22,56−58] Whence, we used the time-dependent viscosity $\eta(t)$, defined as

$$\eta(t) = \int_0^t G(t')\mathrm{d}t' \tag{2}$$

(where $G(t)$ is the time-dependent shear modulus), as a proxy for the bulk mechanics of the polymer blend. As such, $\eta(t)$ was probed at a fixed time t_e and used as a property representative of the polymer dynamics.

Thus, the performance f of a given PBE must be a function of performance metrics λ and $\eta(t_e)$: $f(\lambda,\eta(t_e))$, where improving either metric, assuming that the other remains fixed, will improve the performance. Design of PBEs will result from a maximization of f.

We expand the design space of PBEs as a means to optimize the performance f. As in prior work,[22,23,31,59] we adopt the Stockmayer polymer model,[59−61] a coarse-grained model characterized by freely rotating point dipole moments embedded in each repeat unit of a Kremer−Grest polymer.[62] We show in Figure 1 the elements of this design space. The electrolytes consist of two polymers: a nominally low-molecular-weight polymer (designated as polymer A, shown in turquoise in Figure 1 with the degree of polymerization N_A) and a high-molecular-weight component polymer (B, purple, N_B). Each polymer will be assigned one of two dipole strengths, μ_{lo} and μ_{hi}, the assignment of which is controlled by the parameter γ. We define γ to be unity when μ_{lo} is assigned to

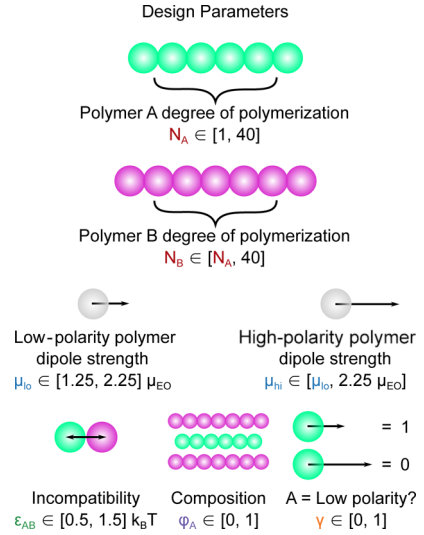

Figure 1. Design parameters (and their ranges) of the Stockmayer PBEs explored in this work.

polymer A. We will include the Lennard-Jones (LJ) cross-interaction energy between polymers A and B, ε_{AB}, which has been shown to influence the miscibility of polymer blends.[31,62−64] Finally, we will vary the relative composition of polymer A $\phi_A = N_A n_A/(N_A n_A + N_B n_B)$, where n_i is the number of chains of polymer type i. In summary, the chosen design parameter vector is $\mathbf{x} = (N_A, N_B, \mu_{lo}, \mu_{hi}, \varepsilon_{AB}, \phi_A, \gamma)^T$, with bounds defined in Figure 1. Each parameter (aside from γ) introduced above has been shown to influence ionic aggregation and polymer dynamics in polymeric materials,[22,23,31,59,65] which in turn have been shown to influence ion transport[22,23,25,27−31,65−67] and the mechanical properties of polymeric materials.[68,69] As a result, we can express the performance as a function of the design parameters: $f(\lambda(\mathbf{x}), \eta(t_e,\mathbf{x})) = f(\mathbf{x})$. Please see the Methods section for all other Stockmayer model details.

Our goal to maximize $f(\mathbf{x})$ is hindered by two issues: (1) the analytical relationship between the design parameters $\mathbf{x}$ and the performance $f(\mathbf{x})$ cannot a priori be expressed, and (2) an Edisonian search of the relatively broad design space may not be practically possible. In the absence of a clear physics-based model, ML has been used to correlate design parameters to material properties to design high-performance materials. One such ML algorithm that can address both issues is Bayesian optimization.[70] Bayesian optimization uses Gaussian process regression to fit a statistical model relating f and $\mathbf{x}$

$$f(\mathbf{x}) \sim \mathcal{N}(\mu(\mathbf{x}), k(\mathbf{x}, \mathbf{x}')) \tag{3}$$

where $\mathcal{N}$ is a normal distribution with mean function $\mu(\mathbf{x})$ describing belief in the relationship between f and $\mathbf{x}$ and the covariance function, or kernel, $k(\mathbf{x},\mathbf{x}')$ describing the uncertainty of that belief. By conditioning this model based on prior performance evaluations, the resultant posterior model can be used to predict subsequent performance evaluations at a given design vector $\mathbf{x}$ tending toward the desired optimum.

To summarize, we explored the use of Bayesian optimization ML techniques in conjunction with molecular dynamics simulations to examine parametric regimes of PBEs which can facilitate optimal combinations of ionic transport and electrolyte mechanical properties. In the Objective Function

https://dx.doi.org/10.1021/acs.macromol.0c01547
Macromolecules 2020, 53, 9449−9459

Choice and Simplification section, we describe in detail the formulation of the performance $f(\mathbf{x})$. We recognize the expense of evaluation of $f(\mathbf{x})$; as a result, we suggest a means to cheapen said function evaluation by replacing $f(\mathbf{x})$ with a proxy performance $f_p(\mathbf{x})$. In the Optimization Results section, optimizing $f_p(\mathbf{x})$, we reveal a trade-off between λ and η and explore the changes in the optimal design vector $\mathbf{x}'$ underpinning such a trade-off. Given these, we probe the physics underlying our results by perturbing elements of $\mathbf{x}'$ and discuss the potential mechanisms in the Physics Underlying Optimized Blends section. In the Conclusions section, we summarize our findings and comment on the value of Bayesian optimization in combination with molecular simulation in materials design.

2. RESULTS AND DISCUSSION

2.1. Objective Function Choice and Simplification. As mentioned in the Introduction section, we first developed an expression for the performance $f(\mathbf{x})$, noting a potential trade-off between λ and η. If we assume a similar level of correlated ionic motion across all design parameters $\mathbf{x}$ (yielding a roughly constant degree of uncorrelated motion α), eq 1 shows that λ becomes proportional to the sum of the cationic and anionic diffusivities (D_c and D_a, respectively). As a result of the inverse correlation between penetrant (namely, ionic) diffusivities D_i and η[71] and the direct correlation between η and the host degree of polymerization N,[18] $\lambda \propto \eta^{-1} \propto N^{-1}$ for unentangled polymers. Thus, λ and η are expected to trade off with each other. Any attempt to optimize polymer electrolyte performance on the basis of these two metrics must identify a Pareto front in which systematic improvement of one metric will result in a degradation of the other.[72]

To this end, the anticipated trade-off between each performance metric can be incorporated into the expression for $f(\mathbf{x})$. An objective function form widely used in multi-objective optimization with a presumed Pareto front is the linear scalarized form

$$f(\mathbf{x}) = w_1 \overline{f}_1(\mathbf{x}) + (1 - w_1)\overline{f}_2(\mathbf{x}) \tag{4}$$

where $\overline{f}_1(\mathbf{x})$ and $\overline{f}_2(\mathbf{x})$ are two scaled performance metrics and $w_1 \in [0, 1]$ is a factor that weights the relative importance of each performance metric. Such a form requires that $\overline{f}_1, \overline{f}_2 \sim O(1)$ to appropriately compare each performance metric. This can be done for performance metric i using a minimum−maximum rescaling

$$\overline{f}_i(\mathbf{x}) = \frac{f_i(\mathbf{x}) - f_{i,\min}}{f_{i,\max} - f_{i,\min}} \tag{5}$$

where $f_i(\mathbf{x})$ is the performance metric i and $f_{i,\min}$ and $f_{i,\max}$ are minimum and maximum values of performance metric i, respectively. To address the assumed scaling of λ and η with N and ensure linearity with $\log(N)$, we chose $f_1(\mathbf{x}) = \log(\lambda)$ and $f_2(\mathbf{x}) = \log(\eta)$. Substituting these definitions and eq 5 into eq 4, we arrive at the final expression of the performance

$$f(\mathbf{x}) = w_\lambda \frac{\log(\lambda(\mathbf{x})/\lambda_{\min})}{\log(\lambda_{\max}/\lambda_{\min})} + (1 - w_\lambda)\frac{\log(\eta(\mathbf{x})/\eta_{\min})}{\log(\eta_{\max}/\eta_{\min})} \tag{6}$$

The maxima and minima of λ and η were determined based on a core set of 29 simulations, discussed in more detail below. Setting $w_\lambda = 1$ ensures full emphasis on transport, whereas setting $w_\lambda = 0$ ensures emphasis only on electrolyte viscosity.

Unfortunately, even within the coarse-grained model adopted for this work, an accurate evaluation of $f(\mathbf{x})$ is computationally expensive because of the long simulations (with potential replicates) needed to determine λ[21−23,31,50,73−77] and η.[78,79] We hypothesized that easier-to-evaluate measures may serve as proxies for λ and η. The ionic diffusion coefficients D_i are proportional to the slope of their mean-squared displacements (MSDs)

$$D_i = \lim_{t\to\infty} \frac{1}{6n_i t} \sum_i^{n_i} \langle \|\mathbf{r}_i(t) - \mathbf{r}_i(0)\|^2 \rangle \tag{7}$$

Such a relationship requires long-time linearity of the MSDs to be accurate. We anticipated that the ionic MSDs at some fixed short time t_0 could serve as potential proxies for λ. In addition, the longest Rouse mode timescales correspond to chain diffusion and are proportional to η.[18] As a result, the polymer relaxation time τ_R derived from the self-part of the intermediate scattering function $S(q, t)$ could serve as a proxy for η. We chose $q = 2\pi/5.0\sigma^{-1}$. The length scale encoded in $S(q,t)$ is approximately the polymers' radius of gyration (see Figure S2C in the Supporting Information) and should capture some of the effects of polymer diffusion.[18]

To ascertain if correlations exist between the performance metrics and the proposed proxies, we simulated 29 samples of Stockmayer electrolytes with randomly chosen design parameters within the ranges specified by Figure 1. The design parameters for these systems can be seen in the Supporting Information, Table S1. To calculate η, simulations with equilibration steps of 1.5×10^5 τ and production steps of 3.75×10^4 τ were carried out, where the characteristic timescale $\tau = m\sigma^2/\varepsilon$, with elements of the pressure tensor reported every 0.0025 τ. As discussed in the Introduction section, $\eta(t_e = 2000\ \tau)$ was calculated by integrating the time-dependent shear modulus.[78,79] Full details for this calculation can be found in the Methods section. All other properties were derived from simulations with equilibration steps of 1.5×10^5 τ and production steps of 5×10^5 τ, in which all particle positions were reported every 0.5 τ. λ was determined using the full length of each simulation using a mixture of long- and short-time statistics, briefly discussed in the Methods section and in more depth in prior work.[21−23,31,50,73−76] The first 5×10^3 τ of these trajectories were treated as a short-run simulation. Using eq 7, the ionic MSDs from these short-run simulations were calculated at $t_0 = 2.5 \times 10^3$. As discussed in the Methods section, τ_R was also extracted from the short-run simulations.

We display the results of these calculations in Figure 2, rescaling all results using eq 5. For simplicity, we fit the data to weighted linear regression models (dashed lines) using a training subset of these data (hollow symbols, corresponding to 80% of the simulations run). We measured their predictivity by calculating the score r^2 on the test set (full symbols). The r^2 values for the transport metrics (Figure 2A) were 0.68 (anion) and 0.33 (cation), indicating moderate and poor predictivity of λ, respectively. To maintain maximal predictivity, the anionic MSD was chosen as the proxy metric for λ. η was moderately predicted by τ_R (Figure 2B, $r^2 = 0.76$). Thus, the proxy performance $f_p(\mathbf{x})$ took on the following form, via substitution of the short-time proxy metrics for their long-time analogues

https://dx.doi.org/10.1021/acs.macromol.0c01547
Macromolecules 2020, 53, 9449−9459

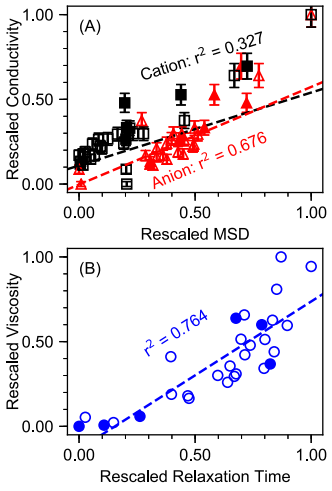

Figure 2. (A) Conductivity λ as a function of cationic (black squares) or anionic (red triangles) short-time MSDs. Error bars indicate one standard deviation. (B) Viscosity $\eta(t_e = 2000\ \tau)$ as a function of polymer relaxation time τ_R. Dashed lines represent the linear regression curve derived from the weighted least squares procedure. Training and test sets for linear regression are represented by hollow and full symbols, respectively. r^2 values indicate predictivity based on test set comparison. The results suggest that λ and η are well correlated with easy-to-calculate proxy measures of the anionic MSD and τ_R.

$$f_p(\mathbf{x};\ w_D) = w_D \frac{\log(\mathrm{MSD}_a(\mathbf{x})/\mathrm{MSD}_{a,\min})}{\log(\mathrm{MSD}_{a,\max}/\mathrm{MSD}_{a,\min})} + (1 - w_D)\frac{\log(\tau_R(\mathbf{x})/\tau_{R,\min})}{\log(\tau_{R,\max}/\tau_{R,\min})} \quad (8)$$

with $w_D \in [0, 1]$ substituted here for w_λ seen in eq 4. The values used to rescale the anionic MSD and τ_R were the minima and maxima proxy values from the set of 29 simulations above.

2.2. Optimization Results. Herein, we report the results of the Bayesian optimization as a function of the emphasis on transport w_D. Using the 29 core simulations described above as the test set for this optimization, a minimum of 15 iterations were carried out to optimize $f_p(\mathbf{x};w_D)$. Each iteration incorporated data from all prior iterations, as detailed in the Supporting Information, eq S7. Importantly, we assigned some measurement error σ_n^2 to each evaluation of $f_p(\mathbf{x};w_D)$ in prior iterations to be equal to 0.1. Three blend electrolytes were simulated per iteration, which were chosen by the method of local penalization.[80] Each of these simulations consisted of an equilibration step of $1.9 \times 10^4\ \tau$ and a production step of $5 \times 10^3\ \tau$, with particle positions reported every $0.5\ \tau$. As shown in Figure S2C, we can see from a sample of runs for $w_D = 0.5$ that the polymer conformations [measured by their radii of gyration $R_g^2(t)$] largely converge (with some fluctuation) during the equilibration run. In addition, as shown in Figure S2, stable energies from a different sample set of production runs further suggest metastability. While neither of these measurements ensures complete equilibration for these simulations, any anticipated error arising from incomplete equilibration was modeled by including the measurement error term $\sigma_n^2 = 0.1$.

The optimizations were considered finished when at least four iterations yielded no improvement in $f_p(\mathbf{x};w_D)$. In Figure 3, we present details of the optimization of the proxy performance $f_p(\mathbf{x};w_D)$ for all w_D. In comparison to the best value of f_p from the core simulation (blue dashed line), one can see that the best value f_p' (red dashed lines) arising from the optimization ranges from being relatively insensitive as a function of simulation number n_s (as in Figure 3C) to quite sensitive (as in Figure 3H). In all cases, f_p' slowly increases with simulation number, eventually plateauing. It can be seen that at least 12 simulations (or 4 iterations) were run after that in which f_p is maximized. When looking at each evaluation of f_p, shown by the black squares, it is clear that the optimization algorithm balances between exploitation (improved best values of $f_p(\mathbf{x})$ with optimization run time) and exploration (evaluating design parameters that ultimately yielded particularly low values of $f_p(\mathbf{x})$). Please see the Supporting Information, Table S2, for a summary of these results. In addition, see the Optimization Implementation section in the Methods section for the algorithm used to perform the optimization and the section in the Supporting Information for further details on model training and acquisition function calculation.

As anticipated, the Bayesian optimization identified a trade-off between ionic transport and electrolyte mechanical properties. We plot in Figure 4A the Pareto front between the anionic MSD and τ_R. Each data point represents the average of the three best f_p evaluations. As the emphasis on

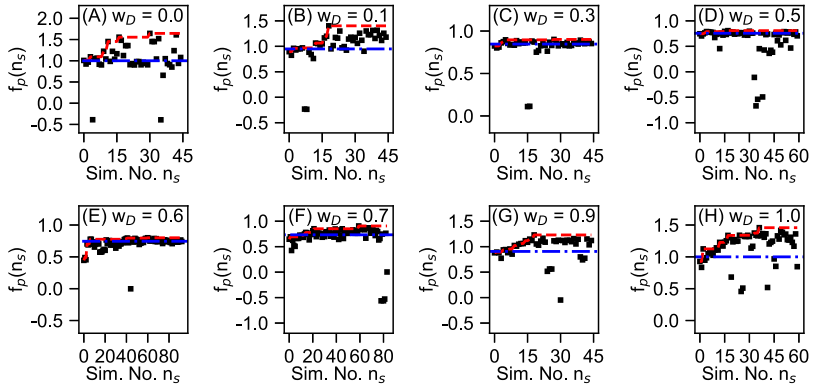

Figure 3. $f_p(\mathbf{x};w_D)$ (black squares) as a function of the number of short-run simulations n_s after core simulations, the best value of $f_p(\mathbf{x};w_D)$ (blue dashed line) of the core simulations, and the best value of $f_p(\mathbf{x};w_D)$ (red dashed line) arising from the optimization itself as a function of the number of short-run simulations. Each panel is for a given w_D value. It can be seen that the optimization values plateau for at least 12 simulations.

https://dx.doi.org/10.1021/acs.macromol.0c01547
Macromolecules 2020, 53, 9449−9459

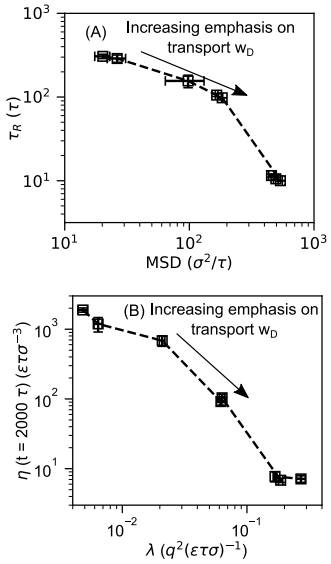

Figure 4. (A) Pareto front between the optimal anionic MSD and polymer relaxation time τ_R, averaged over three best-performing electrolytes. (B) Pareto front between ionic conductivity λ and viscosity η for the best set of design parameters identified by proxy optimization. In both (A) and (B), error bars represent one standard deviation. The results suggest a trade-off between ion transport and electrolyte mechanical properties present even in the true performance metrics.

transport increases, the anionic MSD increases and τ_R decreases over nearly 2 orders of magnitude. The most sensitive region appears for $w_D \in [0.3, 0.7]$ (corresponding to symbols 3−6 from left to right in Figure 4A), suggesting significant transition of electrolyte design parameters over this range.

We sought to confirm the results of the optimization by evaluating the true performance metrics λ and η by performing long-run simulations with the optimal design parameter vector $\mathbf{x}'(w_D)$ (the values which we discuss below). To calculate the conductivity λ, we performed simulations consisting of 1.5×10^5 τ equilibration runs, followed by a 5.0×10^5 τ production run. To calculate the viscosity η, five independent 1.5×10^5 τ equilibration runs were followed by 1.0×10^5 τ production runs. $\eta(t_e = 2000\ \tau)$ was averaged over these five simulations. In Figure 4A, we can see that the results of these simulations reveal a similar trade-off between λ and η over 2 orders of magnitude in Figure 4B. Such a result supports our hypothesis that $f_p(\mathbf{x})$ could serve as a proxy for $f(\mathbf{x})$. As further emphasis of the success of the optimization procedure, the materials appear to become viscoelastic with a plateau regime at lower w_D (see Figure S4 in the Supporting Information), a region which possibly arises from ionic cross-linking.[81−83]

Interestingly, Figure 4A,B shows that ion transport and electrolyte viscosity seem to be somewhat "decoupled" at low w_D. Such a decoupling manifests as a nearly flat curve in which the viscosity changes little while transport increases by nearly an order of magnitude. Similar behavior has been seen recently in metal−ligand-bond-based polymer electrolytes.[54] We investigate below the resulting design parameters from the Bayesian optimization, which may reveal some insight into this phenomenon.

The results for the optimal design parameters $\mathbf{x}(w_D)$ arising from the optimization are shown in Figure 5. We again average over the three best-performing electrolytes. Error bars beyond the ranges of values in Figure 1 do not represent possible solutions within the context of the optimization. We observe that (i) the composition of most blend electrolytes appears to be symmetric in terms of molecular weights and (ii) there is a transition from a polymeric electrolyte to a small-molecule electrolyte at $w_D = 0.6$ (Figure 5A,B). The fact that optimal blends rarely have any molecular weight contrast suggests that electrolytes containing mixtures of the polymer and solvent (such as gel polymer electrolytes[19,84,85]) rarely lie along the Pareto front of electrolyte performance, as defined in this work.

We next turn to the host polymer polarity design parameters, as seen in Figure 5C,D. With high emphasis on material mechanics (low w_D), we observe significant polarity contrast $\mu_{hi} - \mu_{lo}$. However, as emphasis transitions to being on transport (high w_D), $\mu_{hi} - \mu_{lo}$ decreases to negligible levels. When taken in combination with the incompatibility decreasing with w_D (namely, miscibility increasing with w_D), as shown in Figure 5E, we can draw two conclusions. First, at low w_D, the PBE is likely to be a phase-separated material. In previous work, we noted that ions preferentially partitioned to the high-polarity domain and saw that such a partitioning significantly slowed polymer dynamics relative to miscible blends.[31] Such a phenomenon may explain the particular combination of design parameters in Figure 5 at low w_D. Indeed, when we visually investigate the phase behavior for $w_D = 0.1$ in Figure 6, we can see clear domains of high-polarity and low-polarity polymers and a partitioning of cations into the high-polarity phase. Second, at high w_D, the optimal design parameters suggest nearly pure ($N_A = N_B$, $\mu_{lo} \approx \mu_{hi}$), rather

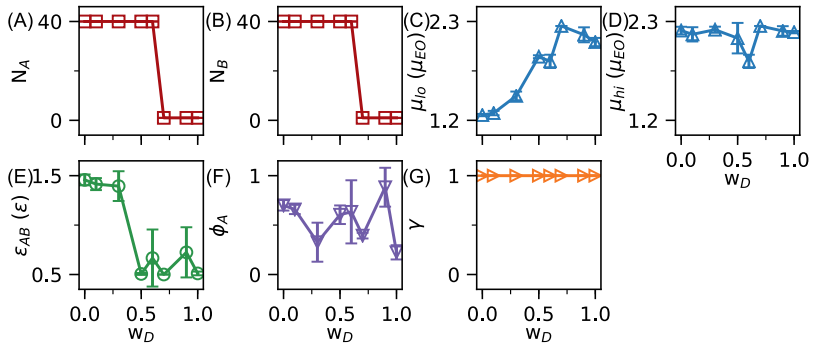

Figure 5. (A) N_A, (B) N_B, (C) μ_{lo}, (D) μ_{hi}, (E) ε_{AB}, (F) ϕ_A, and (G) γ as a function of weighting factor w_D, averaged over the three best-performing electrolytes. Error bars represent one standard deviation and may be hidden behind its respective symbol. Mixed-molecular-weight electrolytes seem to rarely optimize $f_p(\mathbf{x})$.

https://dx.doi.org/10.1021/acs.macromol.0c01547
Macromolecules 2020, 53, 9449−9459

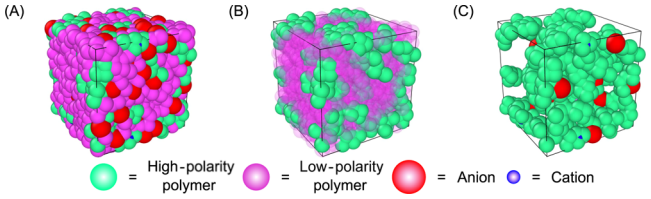

Figure 6. Snapshot of a long-run simulation for the best set of design parameters for w_D = 0.1. The whole system is shown in (A); the polymers only are shown in (B), with one polymer made transparent for clarity; and only the cations and their nearest five neighbors are shown in (C). The high-polarity polymer is shown in blue, the low-polarity polymer in pink, the cations in blue, and the anions in red. Clear domains of each polymer can be seen, and a preference of the cations to interact with the high-polarity polymer is evident.

than blend electrolytes. Such an observation is in conflict with prior small-molecule electrolyte literature studies, in which a blend of high-mobility (typically low polarity) and high-polarity components tend to have faster ionic transport than their pure counterparts.[86] We investigate whether these literature observations hold in relation to our Stockmayer simulations in the next section.

Finally, we turn to the last two parameters, the relative polymer composition ϕ_A and the assignment parameter γ, shown in Figure 5F,G, respectively. γ, which controls the assignment of polarity to one of the polarity hosts, is uniformly set to unity for all w_D. As a result, the nominally low-molecular-weight polymer A is always assigned the low polarity value μ_{lo}. As a result of the molecular weight symmetry, ϕ_A controls the volume fraction of the low-polarity host. Unlike the molecular weight, polarity, and incompatibility design parameters, we observe that there seems to be no clear correlation between these parameters and the evolution of the performance metrics with increasing w_D.

Overall, these results suggest that the molecular weight, polarity, and compatibility design parameters, corresponding to panels A–E in Figure 5, are the most important in the design of high-performance electrolytes in two ways. First, as noted above, they tend to be well correlated with the changes in the performance metrics. Second, their relatively small error bars further emphasize that they cannot be varied much while maintaining high performance. As such, these results suggest that the design of PBEs should focus on these design parameters.

Having reviewed the design parameters in full, we now comment on the possible underlying physical reasons for the decoupling of conduction and viscosity at low w_D, drawing from the results in our previous investigation of PBEs.[31] Such a decoupling may arise from (1) the seeming phase separation of the PBE (Figures 5E and 6) and (2) the gradual transition from a high-polarity contrast electrolyte to a lower contrast material characterized by a singular high-polarity host (Figure 5C,D). We have observed that the overall rate of ionic conduction is significantly slowed in an immiscible blend electrolyte. As $\mu_{lo} \rightarrow \mu_{hi}$ with increasing w_D, the conductivity must increase to that of an electrolyte whose singular host has polarity μ_{hi}.[31] In contrast, we have seen that the low-polarity host has fast dynamics, while the high-polarity host has slow dynamics, which is further penalized by both the presence of the low-polarity host and the immiscibility of the electrolyte. As $\mu_{lo} \rightarrow \mu_{hi}$ with increasing w_D, the low-polarity host dynamics must slow. At the same time, the high-polarity host dynamics must increase.[31] We hypothesize that these two effects incompletely cancel each other out. We propose that these effects underpin our observation of a slower change in the dynamics and viscosity at low w_D in comparison to transport.

2.3. Physics Underlying Optimized Blends. Before we conclude, we seek to perturb the optimal design vectors $\mathbf{x}'$. Such an exercise is important for two reasons. First, such a perturbation allows us to investigate the stability of the Bayesian optimization algorithm's solutions. Second, it helps us to glean physical intuition behind the solution outcomes. To these ends, we investigated the solutions at three w_D values: 0.3, 0.5, and 0.7. These values represent optimizations with mechanical, balanced, and transport emphases, respectively. To perturb the solutions, we chose one parameter to vary, while fixing all others. We performed short-run simulations using the

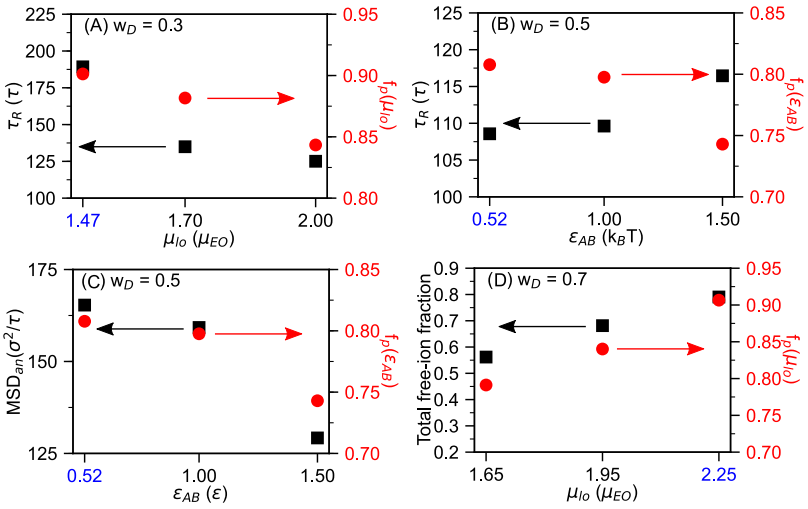

Figure 7. (A) Effect of μ_{lo} on polymer relaxation time τ_R (black squares) and proxy performance $f_p(\mathbf{x})$ (red circles) for w_D = 0.3. (B) Effect of ε_{AB} on polymer relaxation time τ_R (black squares) and proxy performance $f_p(\mathbf{x})$ (red circles) for w_D = 0.5. (C) Effect of ε_{AB} on anionic MSD (black squares) and proxy performance $f_p(\mathbf{x})$ (red circles) for w_D = 0.5. (D) Effect of μ_{lo} on the total free-ion fraction (black squares) and proxy performance $f_p(\mathbf{x})$ (red circles) for w_D = 0.7. The blue tick label represents the optimal value of the explored design parameter. It can be seen that deviating from the identified optimal parameters leads to a reduction in proxy performance.

https://dx.doi.org/10.1021/acs.macromol.0c01547
Macromolecules 2020, 53, 9449–9459

same equilibration and production procedures as those used by the optimization simulations (see the Objective Function Choice and Simplification section). We present the results of these perturbations in Figure 7.

We first begin with $w_D = 0.3$, in which the combination of design parameters suggested a polymeric, immiscible blend electrolyte with a large polarity contrast. In the case of pure polymer electrolytes,[22,23] polymer dynamics slowed the most in electrolytes with high-polarity hosts. Naïvely, one would expect that a similar material would have the best mechanical properties. We investigated such a hypothesis by increasing μ_{lo} in the best-performing blend electrolyte. As shown in Figure 7A, we display the relaxation time τ_R (black squares) and the proxy performance $f_p(\mathbf{x})$ (red triangles) as functions of μ_{lo}. We can see that both τ_R and $f_p(\mathbf{x})$ decrease with μ_{lo}. In recent work, we showed that ions partitioned into the high-polarity phase of immiscible blend electrolytes, which increased with increasing polarity contrast and was correlated with significantly slowed dynamics of the high-polarity polymer.[31] By decreasing polarity contrast, as we have done in the electrolytes underpinning the results seen in Figure 7A, the ions are likely more uniformly distributed throughout the electrolyte, thereby slowing dynamics less overall.

Similar physics influences the optimal design vector for $w_D = 0.5$. We noted a sharp transition from a highly incompatible ($\varepsilon_{AB} \approx 1.5k_BT$) PBE to a highly compatible ($\varepsilon_{AB} \approx 0.5k_BT$) PBE at $w_D = 0.5$. We anticipated that such a transition would be correlated with faster polymer dynamics and faster ionic transport.[31] We varied ε_{AB} to investigate the influence of host compatibility, the results of which are shown in Figure 7B. Consistent with our observations, decreasing polymer compatibility (increasing ε_{AB}) slowed polymer dynamics (increasing polymer relaxation time τ_R), which would have a positive effect of f_p. However, we simultaneously saw a decrease in $f_p(\mathbf{x})$, suggesting a larger increase in the anionic MSD as a trade-off (see Figure 7C). These results suggest that the miscibility of PBEs may be a key design parameter to boost performance, where both transport and the mechanical properties are equally considered.

For $w_D = 0.7$ (emphasis on transport), our results seem to differ from prior experimental results regarding small-molecule electrolytes, which found that a mixture of high-polarity and low-viscosity components promotes fast ionic transport.[86] We hypothesized that our results were consistent with previous simulation findings, in which we observed that small-molecule species were worse at solvating ions than their polymeric counterparts.[23] By reducing the polarity of some of the electrolytes, we expected further increased ionic aggregation to offset a potential increase in dynamics.[22,23] We tested our hypothesis by simulating several electrolytes with lower μ_{lo} values. We calculated the free-ion fraction, defined as the fraction of ions separated by more than 1.25 σ from all counterions. We show in Figure 7D that ionic aggregation increases and that performance decreases when μ_{lo} decreases, as expected. These results suggest that within the Stockmayer model simulated in this work, ionic aggregation in small-molecule electrolytes is quite sensitive to both host polarities. Such a sensitivity translates to decreased electrolyte performance at reduced μ_{lo}. Further investigation to better match the Stockmayer model to experimental reality is required.

3. CONCLUSIONS

In summary, we used Bayesian optimization to examine the potential of PBEs to co-optimize ionic transport and mechanical strength. Recognizing a potential trade-off between these two performance metrics, we developed an objective function that incorporates this trade-off. Further, to speed the optimization process, we correlated proxy performance metrics with the true performance metrics. We demonstrated that both proxy and true performance metrics traded off with each other with increasing emphasis on ionic transport and that materials with a high mechanical emphasis were seemingly viscoelastic. Several key features emerged: host polymer molecular weights sharply decreased, the lower-polarity polymer became more polar, blend electrolyte miscibility increased, and the electrolyte host changed from a blend to a single component. These results suggest that mixed-molecular-weight blend electrolytes, such as gel electrolyte materials, rarely optimize electrolyte performance. Balancing these metrics was better served by having a uniformly high molecular weight when mechanical strength was more strongly desired or a low molecular weight when fast transport was emphasized. When ionic transport was emphasized, our results also showed that pure, high-polarity electrolytes maximized performance. Admittedly, our results differ from related experimental observations, and such discrepancies may arise from a combination of the objective function employed and the ability of our coarse-grained model to reflect atomistic aspects of polarity. Finally, we perturbed the optimal design parameters to investigate the robustness of the optimization procedure and to gain some physical insight into the optimal design parameters. We discovered that perturbations to the design parameters uniformly decreased electrolyte performance. They also highlighted the potential importance of polymer blend miscibility in balancing ionic transport and electrolyte mechanical properties. Despite the limitations of the work presented herein, our study identifies a framework for the combined use of computer simulations and ML approaches which can be used toward the design of higher-performance polymer electrolytes.

4. METHODS

4.1. Stockmayer Model and the Molecular Dynamics Methodology. The Stockmayer model is a simple, coarse-grained model of polar fluids. Each molecule (or repeat unit) contains a freely rotating, point dipole moment. Such a dipole moment encodes the polarity of the species in question, allowing for interactions between the solvent and ions.[59−61] Within this coarse-grained model, we set the characteristic mass $m = 2.99 \times 10^{-26}$ kg, the characteristic energy $\varepsilon = 5.27 \times 10^{-27}$ J, and the characteristic length $\sigma = 4.5$ Å.[59] The nondimensionalized temperature $T^* = k_BT/\varepsilon$ was set to 1.0 for all simulations, where k_B is the Boltzmann constant. All particle masses m_i were also set to = 1.0. Dipolar particles were assigned a rotational inertia $I = 0.25m\sigma^2$. The nondimensionalized proton charge e^* was set according to the following equation

$$e^* = \frac{e}{(4\pi\varepsilon_0\sigma\varepsilon)^{1/2}} = 9.863 \tag{9}$$

where ε_0 is the permittivity of free space. Anionic (a) and cationic (c) charges were chosen to be $q_a = -q_c = -e$. Dipole strengths were set as multiples of that of an ethylene oxide repeat unit at 373 K (1.7 D).[22] Such a quantity was denoted as μ_{EO}, calculated according to the following equation

$$\mu_{EO} = \frac{(1.7\,\mathrm{D})(3.33564 \times 10^{-30}\,\mathrm{Cm/D})}{(4\pi\varepsilon_0\sigma^3\varepsilon)^{1/2}} = 0.775 \tag{10}$$

https://dx.doi.org/10.1021/acs.macromol.0c01547
Macromolecules 2020, 53, 9449−9459

All nonbonded particles interacted through the purely repulsive LJ potential (also known as the Weeks−Chandler−Anderson or WCA potential[87]) and electrostatic interactions. The WCA potential is given as $E_{WCA}(r_{ij})$

$$E_{WCA}(r_{ij}) = 4\varepsilon_{ij}\left[\left(\frac{\sigma_{ij}}{r_{ij}}\right)^{12} - \left(\frac{\sigma_{ij}}{r_{ij}}\right)^{6} + \frac{1}{4}\right], \qquad r_{ij} \le 2^{1/6}\sigma_{ij} \tag{11}$$

where σ_{ij} and ε_{ij} are the LJ radius and energy between particles of type i and j, respectively. σ_{ij} is determined by arithmetically averaging the radii of each particle. Here, the monomeric radii are $\sigma_A = \sigma_B = \sigma$, the cationic radius is $\sigma_c = 0.5\ \sigma$, and the anionic radius is $\sigma_a = 1.5\ \sigma$, all of which were chosen to roughly mimic a poly(ethylene oxide)-based lithium bistriflymide electrolyte in terms of size disparity. ε_{ij} was chosen to be 1.0 k_BT for all pairs of atom types, with the exception of ε_{AB}, as described in the Introductionsection. Ion−ion, ion−dipole, and dipole−dipole interactions were quantified through Coulomb's law, the ion−dipole potential, and the dipole−dipole potential.[88] All electrostatics were directly calculated within a 6 σ range, beyond which they were calculated using Ewald summation.[88,89]

All adjacent particles in a polymer were bonded with the finitely extensible nonlinear elastic (FENE) potential

$$E_{FENE}(r_{ij}) = \frac{1}{2}kR_0^2\ln\left[1 - \left(\frac{r_{ij}}{R_0}\right)^2\right], \qquad r_{ij} \le R_0 \tag{12}$$

The spring constant k and the maximum extension R_0 were chosen to be $30\varepsilon/\sigma^2$ and 1.5σ, respectively.[90]

All simulations were carried out using the Large-scale Atomic/Molecular Massively Parallel Simulator.[91] The number density of all simulations was fixed at 0.85 particles/σ^{-3}. In all simulations, the number of polymer beads was set to approximately 2000. Enough cations and anions were placed in the simulation box to maintain a repeat unit/cation ratio of 16 and electroneutrality. For some of the larger polymers simulated in this work, this corresponds to a box length of ~$4R_g$ (see Figure S2C in the Supporting Information). Each simulation box was packed with random polymer configurations, after which ions were randomly dispersed.

Simulations were performed in the following steps:

1. We minimized using the steepest descent algorithm, followed by the conjugate gradient algorithm. Both were terminated when the relative error fell below 1×10^{-5}.
2. Velocities drawn from a Gaussian distribution with temperature T^* were assigned to all particles for both linear and rotational degrees of freedom.
3. Each system was equilibrated with a timestep of 0.01 τ, where $\tau = m\sigma^2/\varepsilon$ in an NVT ensemble. The temperature was imposed with a Nosé−Hoover thermostat with a time constant of 1.0 τ.[92,93] The length of each equilibration is specified at the point of mention.
4. Each system was run for production with the same parameters for the equilibrations. The length of each production is specified at the point of mention.

4.2. Analyses Performed. *4.2.1. Conductivity.* As described by eq 1, we calculated the ionic conductivities of select simulations. Such a calculation was performed in two parts using a previously described literature procedure.[21−23,31,75,76] First, the ionic diffusion coefficients (D_c and D_a) were calculated using the Einstein relation in eq 7 using the long-time MSDs of each ion type. Second, the degree of uncorrelated motion was estimated using short-time statistics ($t \le 0.05t_{total}$, where t_{total} is the run length of the simulation) of the following equation

$$\alpha(t) = \frac{\sum_{i,j}^{n_{ion}} \langle \{\mathbf{r}_i(t) - \mathbf{r}_i(0)\}\cdot\{\mathbf{r}_j(t) - \mathbf{r}_j(0)\}\rangle}{\sum_{i}^{n_{ion}} \langle \|\mathbf{r}_i(t) - \mathbf{r}_i(0)\|^2\rangle} \tag{13}$$

We calculated the average value $\bar{\alpha}$ using the following equation

$$\bar{\alpha} = \frac{1}{9}\sum_{n=1}^{9} \alpha(t = 0.005{*}n{*}t_{total}) \tag{14}$$

The standard deviation of $\bar{\alpha}$ was also estimated, which was propagated to the final estimate of the standard deviation of the λ.

4.2.2. Viscosity. As described in the main text of the paper, the viscosity η was calculated by initially calculating the time-dependent shear modulus $G(t)$[78,79]

$$G(t) = \frac{V}{10k_BT}\left\langle \sum_{i=1}^{6} P_i(0)P_i(t) \right\rangle \tag{15}$$

where V is the system volume, k_B is the Boltzmann constant, and T is the system temperature. The six pressure elements were related to the elements of the pressure tensor: $P_1 = 2P_{xy}$, $P_2 = 2P_{yz}$, $P_3 = 2P_{xz}$, $P_4 = \frac{4}{3}\left[P_{xx} - \frac{1}{3}(P_{xx} + P_{yy} + P_{zz})\right]$, $P_5 = \frac{4}{3}\left[P_{yy} - \frac{1}{3}(P_{xx} + P_{yy} + P_{zz})\right]$, and $P_6 = \frac{4}{3}\left[P_{zz} - \frac{1}{3}(P_{xx} + P_{yy} + P_{zz})\right]$. Each element of the pressure tensor $P_{\alpha\beta}$ was calculated according to the virial equation

$$P_{\alpha\beta} = \frac{1}{V}\left(\sum_i m_i v_{\alpha i}v_{\beta i} + 0.5\sum_{i\neq j} r_{\alpha ij}F_{\beta ij}\right) \tag{16}$$

where m_i is the mass of particle i, $v_{\alpha i}$ is the velocity of particle i in direction α, $r_{\alpha ij}$ is the distance between particles i and j in direction α, and $F_{\beta ij}$ is the force acting on particle i due to its interaction with particle j in direction β. η was calculated by integrating $G(t)$[78,79]

$$\eta = \int_0^\infty G(t)\mathrm{d}t \tag{17}$$

Formally, the upper bound of this integral is chosen such that $G(t) \to 0$. However, because of the computational expense needed for simulations to accurately obtain η, particularly for polymeric materials, the integral was truncated at $t_e = 2000\ \tau$. As such, the viscosity calculated herein serves as an incomplete averaging of the simulated materials' response to a shear stress.

4.2.3. Polymer Relaxation Time. The self-part of the intermediate scattering function $S(q,t)$ was calculated according to the following equation

$$S(q, t) = \frac{1}{n_{mon}}\sum_{i}^{n_{mon}}\left\langle \frac{\sin(q\|\mathbf{r}_i(t) - \mathbf{r}_i(0)\|)}{q\|\mathbf{r}_i(t) - \mathbf{r}_i(0)\|}\right\rangle \tag{18}$$

where $q = 2\pi/5.0\ \sigma^{-1}$ and n_{mon} is the number of monomers in the system. $S(q,t)$ was fit to a stretched exponential[94]

$$S(q, t) = \exp\left[-\left(\frac{t}{t^*}\right)^{\beta}\right] \tag{19}$$

where t^* is the characteristic timescale and β is the stretching exponential. The polymer relaxation time τ_R was calculated using the following equation

$$\tau_R = t^*\Gamma\left(1 + \frac{1}{\beta}\right) \tag{20}$$

where $\Gamma(x)$ is the gamma function with argument x.

4.2.4. Optimization Implementation. Bayesian optimization was carried out using the design-of-experiments function (GPyOpt.methods.BayesianOptimization.suggest_next_locations()) in the Python package GPyOpt.[95] As described in the main text of this work, 29 simulations were carried out form the original test set $\mathbf{y}_{MSD,0}$ and $\mathbf{y}_{\tau_R,0}$, which were 29-element-long vectors containing the anionic MSDs and polymer relaxation times, respectively, and X_0, which contained the design parameters. The initial kernel $\mathcal{K}_0$ was the Mátern 5/2 covariance function with arbitrary parameters $\sigma_0^2 = 1.0$and $I_0 = (1.0, ..., 1.0)^T$ added to a measurement uncertainty, described above, with $\sigma_n^2 = 0.1$. It had the following form

https://dx.doi.org/10.1021/acs.macromol.0c01547
Macromolecules 2020, 53, 9449−9459

$$\mathcal{K}(X_0, X_0) = K(X_0, X_0) + \sigma_n^2 I \quad (21)$$

The following procedure at optimization step i was implemented

1. Following eqs S4−S7 from the Supporting Information, convert $\mathbf{y}_{\mathrm{MSD},i-1}$ and $\mathbf{y}_{\mathrm{tau_R},i-1}$ to $\mathbf{f}_{\mathrm{p},i-1}$.
2. Initialize the kernel $\mathcal{K}_{i-1}(X_{i-1}, X_{i-1})$ using the conditioned kernel parameters σ_{i-1}^2 and $\boldsymbol{l}_{i-1}$.
3. Pass the domain (given in Figure 1), constraints (given in Figure 1), $\mathcal{K}_{i-1}(X_{i-1}, X_{i-1})$, and the desired acquisition function (here, the expected improvement acquisition function, see eq S10) to the Bayesian optimization object in GPyOpt. Assume a mean function $\mu_{i-1} = 0$. This step conditions the prior distribution to the posterior distribution, described above.
4. Report the conditioned parameters $\sigma_i^2$and $\boldsymbol{l}_i$ to a data file.
5. Use the initialized Bayesian optimization object with the local penalization method to suggest three simulations with design parameters $X_i^* = (\mathbf{x}_{1,i}^* \mathbf{x}_{2,i}^* \mathbf{x}_{3,i}^*)$. Report $X_i = (X_{i-1}X_i^*)$ to a data file.
6. Run short simulations as described.
7. Calculate $\mathbf{y}_{\mathrm{MSD},i}^*$ and $\mathbf{y}_{\tau_R,i}$. Report $\mathbf{y}_{\mathrm{MSD},i} = \begin{pmatrix} \mathbf{y}_{\mathrm{MSD},i-1} \\ \mathbf{y}_{\mathrm{MSD},i}^* \end{pmatrix}$ and $\mathbf{y}_{\tau_R,i} = \begin{pmatrix} \mathbf{y}_{\tau_R,i-1} \\ \mathbf{y}_{\tau_R,i}^* \end{pmatrix}$ to data.

The above procedure is repeated until both $i \geq 15$ (45 short-run simulations ran at the minimum) and the maximum objective value f' is constant for at least 4 iterations (12 short-run simulations of no improvement in the objective function).

■ ASSOCIATED CONTENT

Supporting Information

The Supporting Information is available free of charge at https://pubs.acs.org/doi/10.1021/acs.macromol.0c01547.

Core simulation parameters; sample core simulation MSDs and $S(q,t)$; Bayesian optimization theory; optimization run radius of gyrations and simulation energies for $w_D = 0.5$; $f_p(\mathbf{x})$ evaluations; long-run simulation results of $G(t)$ for optimal design parameters; and perturbation MSD complement (PDF)

■ AUTHOR INFORMATION

Corresponding Author

Venkat Ganesan − *McKetta Department of Chemical Engineering, The University of Texas at Austin, Austin 78712, Texas, United States;* orcid.org/0000-0003-3899-5843; Email: venkat@che.utexas.edu

Authors

Bill K. Wheatle − *McKetta Department of Chemical Engineering, The University of Texas at Austin, Austin 78712, Texas, United States;* orcid.org/0000-0003-0550-4905

Erick F. Fuentes − *McKetta Department of Chemical Engineering, The University of Texas at Austin, Austin 78712, Texas, United States*

Nathaniel A. Lynd − *McKetta Department of Chemical Engineering, The University of Texas at Austin, Austin 78712, Texas, United States;* orcid.org/0000-0003-3010-5068

Complete contact information is available at: https://pubs.acs.org/10.1021/acs.macromol.0c01547

Notes

The authors declare no competing financial interest.

■ ACKNOWLEDGMENTS

This work was supported by funding from both the National Science Foundation (grants DMR-1721512 and CBET-17069698) and the Robert A. Welch Foundation (grants F-1599 and F-1904). High-performance computing resources provided by the Texas Advanced Computing Center at the University of Texas at Austin were used to generate the results in this work.

■ REFERENCES

(1) Mai, T.; Sandor, D.; Wiser, R.; Schneider, T. *Renewable Electricity Futures Study: Executive Summary*, 2012.

(2) McLaren, J.; Laws, N.; Anderson, K.; DiOrio, N.; Miller, H. Solar-plus-storage economics: What works where, and why? *Electr. J.* **2019**, *32*, 28−46.

(3) Ziegler, M. S.; Mueller, J. M.; Pereira, G. D.; Song, J.; Ferrara, M.; Chiang, Y.-M.; Trancik, J. E. Storage Requirements and Costs of Shaping Renewable Energy Toward Grid Decarbonization. *Joule* **2019**, *3*, 2134−2153.

(4) Barai, P.; Higa, K.; Srinivasan, V. Lithium dendrite growth mechanisms in polymer electrolytes and prevention strategies. *Phys. Chem. Chem. Phys.* **2017**, *19*, 20493−20505.

(5) Meesala, Y.; Jena, A.; Chang, H.; Liu, R.-S. Recent Advancements in Li-Ion Conductors for All-Solid-State Li-Ion Batteries. *ACS Energy Lett.* **2017**, *2*, 2734−2751.

(6) Liu, J.; et al. Pathways for practical high-energy long-cycling lithium metal batteries. *Nat. Energy* **2019**, *4*, 180−186.

(7) Lopez, J.; Mackanic, D. G.; Cui, Y.; Bao, Z. Designing polymers for advanced battery chemistries. *Nat. Rev. Mater.* **2019**, *4*, 312−330.

(8) Chazalviel, J.-N. Electrochemical Aspects of the Generation of Ramified Metallic Electrodeposits. *Phys. Rev. A* **1990**, *42*, 7355−7367.

(9) Monroe, C.; Newman, J. The impact of elastic deformation on deposition kinetics at lithium/polymer interfaces. *J. Electrochem. Soc.* **2005**, *152*, A396−404.

(10) Buss, H. G.; Chan, S. Y.; Lynd, N. A.; McCloskey, B. D. Nonaqueous Polyelectrolyte Solutions as Liquid Electrolytes with High Lithium Ion Transference Number and Conductivity. *ACS Energy Lett.* **2017**, *2*, 481−487.

(11) Fong, K. D.; Self, J.; Diederichsen, K. M.; Wood, B. M.; McCloskey, B. D.; Persson, K. A. Ion Transport and the True Transference Number in Nonaqueous Polyelectrolyte Solutions for Lithium Ion Batteries. *ACS Cent. Sci.* **2019**, *5*, 1250−1260.

(12) Diederichsen, K. M.; McCloskey, B. D. Electrolyte additives to enable nonaqueous polyelectrolyte solutions for lithium ion batteries. *Mol. Syst. Des. Eng.* **2020**, *5*, 91−96.

(13) Du, D.; Hu, X.; Zeng, D.; Zhang, Y.; Sun, Y.; Li, J.; Cheng, H. Water-Insoluble Side-Chain-Grafted Single Ion Conducting Polymer Electrolyte for Long-Term Stable Lithium Metal Secondary Batteries. *ACS Appl. Energy Mater.* **2020**, *3*, 1128−1138.

(14) Villaluenga, I.; Inceoglu, S.; Jiang, X.; Chen, X. C.; Chintapalli, M.; Wang, D. R.; Devaux, D.; Balsara, N. P. Nanostructured Single-Ion-Conducting Hybrid Electrolytes Based on Salty Nanoparticles and Block Copolymers. *Macromolecules* **2017**, *50*, 1998−2005.

(15) Inceoglu, S.; Rojas, A. A.; Devaux, D.; Chen, X. C.; Stone, G. M.; Balsara, N. P. Morphology-conductivity relationship of single-ion-conducting block copolymer electrolytes for lithium batteries. *ACS Macro Lett.* **2014**, *3*, 510−514.

(16) Cox, W. P.; Nielsen, L. E.; Keeney, R. Dynamic viscosity and shear modulus of molten polystyrene as a function of molecular weight. *J. Polym. Sci.* **1957**, *26*, 365−374.

(17) Geng, H. Z.; Rosen, R.; Zheng, B.; Shimoda, H.; Fleming, L.; Liu, J.; Zhou, O. Fabrication and properties of composites of poly(ethylene oxide) and functionalized carbon nanotubes. *Adv. Mater.* **2002**, *14*, 1387−1390.

(18) Rubinstein, M.; Colby, R. H. *Polymer Physics*; Oxford University Press: Oxford, England, U.K., 2003.

(19) Aziz, S. B.; Woo, T. J.; Kadir, M. F. Z.; Ahmed, H. M. A conceptual review on polymer electrolytes and ion transport models. *J. Sci. Adv. Mater. Devices* **2018**, *3*, 1−17.
(20) Barteau, K. P. Poly(Glycidyl Ether)-Based Battery Electrolytes: Correlating Polymer Properties to Ion Transport. Ph.D. Thesis, University of California, Santa Barbara, 2015.
(21) Wheatle, B. K.; Keith, J. R.; Mogurampelly, S.; Lynd, N. A.; Ganesan, V. Influence of Dielectric Constant on Ionic Transport in Polyether-Based Electrolytes. *ACS Macro Lett.* **2017**, *6*, 1362−1367.
(22) Wheatle, B. K.; Lynd, N. A.; Ganesan, V. Effect of Polymer Polarity on Ion Transport: A Competition between Ion Aggregation and Polymer Segmental Dynamics. *ACS Macro Lett.* **2018**, *7*, 1149−1154.
(23) Wheatle, B. K.; Fuentes, E. F.; Lynd, N. A.; Ganesan, V. Influence of Host Polarity on Correlating Salt Concentration, Molecular Weight, and Molar Conductivity in Polymer Electrolytes. *ACS Macro Lett.* **2019**, *8*, 888−892.
(24) Zhang, H.; Chen, F.; Lakuntza, O.; Oteo, U.; Qiao, L.; Martinez-Ibañez, M.; Zhu, H.; Carrasco, J.; Forsyth, M.; Armand, M. Inside Cover: Suppressed Mobility of Negative Charges in Polymer Electrolytes with an Ether-Functionalized Anion (Angew. Chem. Int. Ed. 35/2019). *Angew. Chem., Int. Ed.* **2019**, *58*, 11926.
(25) Barteau, K. P.; Wolffs, M.; Lynd, N. A.; Fredrickson, G. H.; Kramer, E. J.; Hawker, C. J. Allyl Glycidyl Ether-Based Polymer Electrolytes for Room Temperature Lithium Batteries. *Macromolecules* **2013**, *46*, 8988−8994.
(26) Bhandary, R.; Schönhoff, M. Polymer effect on lithium ion dynamics in gel polymer electrolytes: Cationic versus acrylate polymer. *Electrochim. Acta* **2015**, *174*, 753−761.
(27) O'Reilly, M. V.; Masser, H.; King, D. R.; Painter, P. C.; Colby, R. H.; Winey, K. I.; Runt, J. Ionic Aggregate Dissolution and Conduction in a Plasticized Single-Ion Polymer Conductor. *Polymer* **2015**, *59*, 133−143.
(28) Sun, J.; Stone, G. M.; Balsara, N. P.; Zuckermann, R. N. Structure-Conductivity Relationship for Peptoid-Based PEO-Mimetic Polymer Electrolytes. *Macromolecules* **2012**, *45*, 5151−5156.
(29) Teran, A. A.; Tang, M. H.; Mullin, S. A.; Balsara, N. P. Effect of Molecular Weight on Conductivity of Polymer Electrolytes. *Solid State Ionics* **2011**, *203*, 18−21.
(30) Timachova, K.; Watanabe, H.; Balsara, N. P. Effect of Molecular Weight and Salt Concentration on Ion Transport and the Transference Number in Polymer Electrolytes. *Macromolecules* **2015**, *48*, 7882−7888.
(31) Wheatle, B. K.; Lynd, N. A.; Ganesan, V. Effect of Host Incompatibility and Polarity Contrast on Ion Transport in Ternary Polymer-Polymer-Salt Blend Electrolytes. *Macromolecules* **2020**, *53*, 875−884.
(32) Rojas, A. A.; Thakker, K.; McEntush, K. D.; Inceoglu, S.; Stone, G. M.; Balsara, N. P. Dependence of Morphology, Shear Modulus, and Conductivity on the Composition of Lithiated and Magnesiated Single-Ion-Conducting Block Copolymer Electrolytes. *Macromolecules* **2017**, *50*, 8765−8776.
(33) Le, T.; Epa, V. C.; Burden, F. R.; Winkler, D. A. Quantitative Structure-Property Relationship Modeling of Diverse Materials Properties. *Chem. Rev.* **2012**, *112*, 2889−2919.
(34) Chen, C.; Zuo, Y.; Ye, W.; Li, X.; Deng, Z.; Ong, S. P. A Critical Review of Machine Learning of Energy Materials. *Adv. Energy Mater.* **2020**, *10*, 1903242.
(35) Toyao, T.; Maeno, Z.; Takakusagi, S.; Kamachi, T.; Takigawa, I.; Shimizu, K.-i. Machine Learning for Catalysis Informatics: Recent Applications and Prospects. *ACS Catal.* **2020**, *10*, 2260−2297.
(36) Lin, T.-S.; Coley, C. W.; Mochigase, H.; Beech, H. K.; Wang, W.; Wang, Z.; Woods, E.; Craig, S. L.; Johnson, J. A.; Kalow, J. A.; Jensen, K. F.; Olsen, B. D. BigSMILES: A Structurally-Based Line Notation for Describing Macromolecules. *ACS Cent. Sci.* **2019**, *5*, 1523−1531.
(37) Zhou, M.; Vassallo, A.; Wu, J. Toward the inverse design of MOF membranes for efficient D2/H2 separation by combination of physics-based and data-driven modeling. *J. Membr. Sci.* **2020**, *598*, 117675.
(38) Orupattur, N. V.; Mushrif, S. H.; Prasad, V. Catalytic materials and chemistry development using a synergistic combination of machine learning and ab initio methods. *Comput. Mater. Sci.* **2020**, *174*, 109474.
(39) Pitera, J. W.; Chodera, J. D. On the use of experimental observations to bias simulated ensembles. *J. Chem. Theory Comput.* **2012**, *8*, 3445−3451.
(40) Le, T. C.; Winkler, D. A. Discovery and Optimization of Materials Using Evolutionary Approaches. *Chem. Rev.* **2016**, *116*, 6107−6132.
(41) Jackson, N. E.; Webb, M. A.; de Pablo, J. J. Recent advances in machine learning towards multiscale soft materials design. *Curr. Opin. Chem. Eng.* **2019**, *23*, 106−114.
(42) Pruksawan, S.; Lambard, G.; Samitsu, S.; Sodeyama, K.; Naito, M. Prediction and optimization of epoxy adhesive strength from a small dataset through active learning. *Sci. Technol. Adv. Mater.* **2019**, *20*, 1010−1021.
(43) Sivaraman, G.; Jackson, N. E.; Sanchez-Lengeling, B.; Vazquez-Mayagoitia, A.; Aspuru-Guzik, A.; Vishwanath, V.; de Pablo, J. J. A machine learning workflow for molecular analysis: application to melting points. *Mach. Learn. Sci. Technol.* **2020**, *1*, 02501.
(44) Patra, A.; Batra, R.; Chandrasekaran, A.; Kim, C.; Huan, T. D.; Ramprasad, R. A multi-fidelity information-fusion approach to machine learn and predict polymer bandgap. *Comput. Mater. Sci.* **2020**, *172*, 109286.
(45) Linker, T. M.; Tiwari, S.; Kumazoe, H.; Fukushima, S.; Kalia, R. K.; Nakano, A.; Ramprasad, R.; Shimojo, F.; Vashishta, P. Field-Induced Carrier Localization Transition in Dielectric Polymers. *J. Phys. Chem. Lett.* **2020**, *11*, 352−358.
(46) Hatakeyama-Sato, K.; Tezuka, T.; Umeki, M.; Oyaizu, K. AI-Assisted Exploration of Superionic Glass-Type Li+ Conductors with Aromatic Structures. *J. Am. Chem. Soc.* **2020**, *142*, 3301−3305.
(47) Barnett, J. W.; Bilchak, C. R.; Wang, Y.; Benicewicz, B. C.; Murdock, L. A.; Bereau, T.; Kumar, S. K. Designing exceptional gas-separation polymer membranes using machine learning. *Sci. Adv.* **2020**, *6*, No. eaaz4301.
(48) Wang, Y.; Xie, T.; France-Lanord, A.; Berkley, A.; Johnson, J. A.; Shao-Horn, Y.; Grossman, J. C. Toward Designing Highly Conductive Polymer Electrolytes by Machine Learning Assisted Coarse-Grained Molecular Dynamics. *Chem. Mater.* **2020**, *32*, 4144−4151.
(49) Chandrasekaran, A.; Kim, C.; Venkatram, S.; Ramprasad, R. A Deep Learning Solvent-Selection Paradigm Powered by a Massive Solvent/Nonsolvent Database for Polymers. *Macromolecules* **2020**, *53*, 4764−4769.
(50) Borodin, O.; Gorecki, W.; Smith, G. D.; Armand, M. Molecular Dynamics Simulation and Pulsed-Field Gradient NMR Studies of Bis(fluorosulfonyl)imide (FSI) and Bis[(trifluoromethyl)sulfonyl]-imide (TFSI)-Based Ionic Liquids. *J. Phys. Chem. B* **2010**, *114*, 6786−6798.
(51) Mogurampelly, S.; Keith, J. R.; Ganesan, V. Mechanisms Underlying Ion Transport in Polymerized Ionic Liquids. *J. Am. Chem. Soc.* **2017**, *139*, 9511−9514.
(52) Keith, J. R.; Mogurampelly, S.; Aldukhi, F.; Wheatle, B. K.; Ganesan, V. Influence of Molecular Weight on Ion-Transport Properties of Polymeric Ionic Liquids. *Phys. Chem. Chem. Phys.* **2017**, *19*, 29134−29145.
(53) Fu, Y.; Bocharova, V.; Ma, M.; Sokolov, A. P.; Sumpter, B. G.; Kumar, R. Effects of Counterion Size and Backbone Rigidity on the Dynamics of Ionic Polymer Melts and Glasses. *Phys. Chem. Chem. Phys.* **2017**, *19*, 27442−27451.
(54) Schauser, N. S.; Sanoja, G. E.; Bartels, J. M.; Jain, S. K.; Hu, J. G.; Han, S.; Walker, L. M.; Helgeson, M. E.; Seshadri, R.; Segalman, R. A. Decoupling Bulk Mechanics and Mono- and Multivalent Ion Transport in Polymers Based on Metal-Ligand Coordination. *Chem. Mater.* **2018**, *30*, 5759−5769.

https://dx.doi.org/10.1021/acs.macromol.0c01547
Macromolecules 2020, 53, 9449−9459

(55) Bocharova, V.; Sokolov, A. P. Perspectives for Polymer Electrolytes: A View from Fundamentals of Ionic Conductivity. *Macromolecules* **2020**, *53*, 4141−4157.
(56) Mongcopa, K. I. S.; Tyagi, M.; Mailoa, J. P.; Samsonidze, G.; Kozinsky, B.; Mullin, S. A.; Gribble, D. A.; Watanabe, H.; Balsara, N. P. Relationship between Segmental Dynamics Measured by Quasi-Elastic Neutron Scattering and Conductivity in Polymer Electrolytes. *ACS Macro Lett.* **2018**, *7*, 504−508.
(57) Mongcopa, K. I. S.; Gribble, D. A.; Loo, W. S.; Tyagi, M.; Mullin, S. A.; Balsara, N. P. Segmental Dynamics Measured by Quasi-Elastic Neutron Scattering and Ion Transport in Chemically Distinct Polymer Electrolytes. *Macromolecules* **2020**, *53*, 2406−2411.
(58) Webb, M. A.; Yamamoto, U.; Savoie, B. M.; Wang, Z.-G.; Miller, T. F. Globally Suppressed Dynamics in Ion-Doped Polymers. *ACS Macro Lett.* **2018**, *7*, 734−738.
(59) Liu, L.; Nakamura, I. Solvation Energy of Ions in Polymers: Effects of Chain Length and Connectivity on Saturated Dipoles Near Ions. *J. Phys. Chem. B* **2017**, *121*, 3142−3150.
(60) Stockmayer, W. H. Second virial coefficients of polar gases. *J. Chem. Phys.* **1941**, *9*, 398−402.
(61) Stockmayer, W. H. Dielectric Dispersion in Solutions of Flexible Polymers. *Pure Appl. Chem.* **1967**, *15*, 539−554.
(62) Grest, G. S.; Lacasse, M. D.; Kremer, K.; Gupta, A. M. Efficient continuum model for simulating polymer blends and copolymers. *J. Chem. Phys.* **1996**, *105*, 10583−10594.
(63) Gartner, T. E.; Kubo, T.; Seo, Y.; Tansky, M.; Hall, L. M.; Sumerlin, B. S.; Epps, T. H. Domain Spacing and Composition Profile Behavior in Salt-Doped Cyclic vs Linear Block Polymer Thin Films: A Joint Experimental and Simulation Study. *Macromolecules* **2017**, *50*, 7169−7176.
(64) Seo, Y.; Shen, K.-H.; Brown, J. R.; Hall, L. M. Role of Solvation on Diffusion of Ions in Diblock Copolymers: Understanding the Molecular Weight Effect through Modeling. *J. Am. Chem. Soc.* **2019**, *141*, 18455−18466.
(65) Brooks, D. J.; Merinov, B. V.; Goddard, W. A.; Kozinsky, B.; Mailoa, J. Atomistic Description of Ionic Diffusion in PEO-LiTFSI: Effect of Temperature, Molecular Weight, and Ionic Concentration. *Macromolecules* **2018**, *51*, 8987−8995.
(66) Thelen, J. L.; Inceoglu, S.; Venkatesan, N. R.; Mackay, N. G.; Balsara, N. P. Relationship between Ion Dissociation, Melt Morphology, and Electrochemical Performance of Lithium and Magnesium Single-Ion Conducting Block Copolymers. *Macromolecules* **2016**, *49*, 9139−9147.
(67) Sarapas, J. M.; Tew, G. N. Poly(ether-thioethers) by Thiol-Ene Click and Their Oxidized Analogues as Lithium Polymer Electrolytes. *Macromolecules* **2016**, *49*, 1154−1162.
(68) Hou, J.-X.; Svaneborg, C.; Everaers, R.; Grest, G. S. Stress relaxation in entangled polymer melts. *Phys. Rev. Lett.* **2010**, *105*, 1−4.
(69) Ge, T.; Grest, G. S.; Rubinstein, M. Nanorheology of Entangled Polymer Melts. *Phys. Rev. Lett.* **2018**, *120*, 057801.
(70) Rasmussen, C. E.; Williams, C. K. I. *Gaussian Processes for Machine Learning*; The MIT Press: Cambridge, Massachusetts, 2006.
(71) Deen, W. M. *Analysis of Transport Phenomena*; Oxford University Press: New York, 1998.
(72) Mietinnen, K. *Nonlinear Multiobjective Optimization*; Kluwer Academic Publishers Group: Norwell, MA, 1998.
(73) Lesch, V.; Jeremias, S.; Moretti, A.; Passerini, S.; Heuer, A.; Borodin, O. A Combined Theoretical and Experimental Study of the Influence of Different Anion Ratios on Lithium Ion Dynamics in Ionic Liquids. *J. Phys. Chem. B* **2014**, *118*, 7367−7375.
(74) Li, Z.; Smith, G. D.; Bedrov, D. Li^+ Solvation and Transport Properties in Ionic Liquid/Lithium Salt Mixtures: A Molecular Dynamics Simulation Study. *J. Phys. Chem. B* **2012**, *116*, 12801−12809.
(75) Picálek, J.; Kolafa, J. Molecular Dynamics Study of Conductivity of Ionic Liquids: The Kohlrausch Law. *J. Mol. Liq.* **2007**, *134*, 29−33.
(76) Mogurampelly, S.; Ganesan, V. Effect of Nanoparticles on Ion Transport in Polymer Electrolytes. *Macromolecules* **2015**, *48*, 2773−2786.
(77) Zhang, Z.; Wheatle, B. K.; Krajniak, J.; Keith, J. R.; Ganesan, V. Ion Mobilities, Transference Numbers, and Inverse Haven Ratios of Polymeric Ionic Liquids. *ACS Macro Lett.* **2020**, *9*, 84−89.
(78) Cui, S. T.; Cummings, P. T.; Cochran, H. D. The calculation of the viscosity from the autocorrelation function using molecular and atomic stress tensors. *Mol. Phys.* **1996**, *88*, 1657−1664.
(79) Nasrabadi, A. T.; Ganesan, V. Structure and Transport Properties of Lithium-Doped Aprotic and Protic Ionic Liquid Electrolytes: Insights from Molecular Dynamics Simulations. *J. Phys. Chem. B* **2019**, *123*, 5588−5600.
(80) González, J.; Dai, Z.; Hennig, P.; Lawrence, N. Batch bayesian optimization via local penalization. *Proceedings of the 19th International Conference on Artificial Intelligence and Statistics, AISTATS*, 2016; pp 648−657.
(81) Xue, Z.; He, D.; Xie, X. Poly(ethylene oxide)-based Electrolytes for Lithium-ion Batteries. *J. Mater. Chem. A* **2015**, *3*, 19218−19253.
(82) Wang, A.; Liu, X.; Wang, S.; Chen, J.; Xu, H.; Xing, Q.; Zhang, L. Polymeric Ionic Liquid Enhanced All-Solid-State Electrolyte Membrane for High-Performance Lithium-Ion Batteries. *Electrochim. Acta* **2018**, *276*, 184−193.
(83) Abbott, L. J.; Lawson, J. W. Effects of Side Chain Length on Ionic Aggregation and Dynamics in Polymer Single-Ion Conductors. *Macromolecules* **2019**, *52*, 7456−7467.
(84) Fan, L.; Wei, S.; Li, S.; Li, Q.; Lu, Y. Recent Progress of the Solid-State Electrolytes for High-Energy Metal-Based Batteries. *Adv. Energy Mater.* **2018**, *8*, 1702657−31.
(85) Hu, Z.; Chen, J.; Guo, Y.; Zhu, J.; Qu, X.; Niu, W.; Liu, X. Fire-resistant, high-performance gel polymer electrolytes derived from poly(ionic liquid)/P(VDF-HFP) composite membranes for lithium ion batteries. *J. Membr. Sci.* **2020**, *599*, 117827.
(86) Xu, K. Nonaqueous liquid electrolytes for lithium-based rechargeable batteries. *Chem. Rev.* **2004**, *104*, 4303−4418.
(87) Weeks, J. D.; Chandler, D.; Andersen, H. C. Role of repulsive forces in determining the equilibrium structure of simple liquids. *J. Chem. Phys.* **1971**, *54*, 5237−5247.
(88) Toukmaji, A.; Sagui, C.; Board, J.; Darden, T. Efficient particle-mesh Ewald based approach to fixed and induced dipolar interactions. *J. Chem. Phys.* **2000**, *113*, 10913−10927.
(89) In 'T Veld, P. J.; Ismail, A. E.; Grest, G. S. Application of Ewald summations to long-range dispersion forces. *J. Chem. Phys.* **2007**, *127*, 144711.
(90) Kremer, K.; Grest, G. S. Dynamics of entangled linear polymer melts: A molecular-dynamics simulation. *J. Chem. Phys.* **1990**, *92*, 5057−5086.
(91) Plimpton, S. Fast Parallel Algorithms for Short-Range Molecular Dynamics. *J. Comput. Phys.* **1995**, *117*, 1−19.
(92) Nosé, S. A Unified Formulation of the Constant Temperature Molecular Dynamics Methods. *J. Chem. Phys.* **1984**, *81*, 511−519.
(93) Hoover, W. G. Canonical Dynamics: Equilibrium Phase-Space Distributions. *Phys. Rev. A* **1985**, *31*, 1695−1697.
(94) Williams, G.; Watts, D. C. Non-Symmetrical Dielectric Relaxation Behaviour Arising from a Simple Empirical Decay Function. *Trans. Faraday Soc.* **1970**, *66*, 80−85.
(95) Authors, T. G. *GPyOpt*, 2016.

https://dx.doi.org/10.1021/acs.macromol.0c01547
Macromolecules 2020, 53, 9449−9459